Anisotropic dry friction with non-convex force reservoirs: modeling and experiments

Simon V. Walker* and Remco I. Leine*
Institute for Nonlinear Mechanics, University of Stuttgart, Germany

Summary. In this paper an anisotropic dry friction force law allowing for non-convex force reservoirs is formulated using tools from convex analysis and the frictional behavior of an anisotropic surface is studied experimentally. While conventional set-valued force laws have the capability to describe the non-smooth behavior of stick and slip, they are limited to convex friction force reservoirs. Since theoretical considerations and experimental results indicate the existence of non-convex force reservoirs, we present a normal cone inclusion force law with two independent sets which enables the use of non-convex star-shaped force reservoirs. A stability analysis proves that the force law is capable of causing anisotropic friction induced instability. The described force law with the experimentally determined data results in an accurate representation of anisotropic frictional behavior.

Introduction

The frictional properties of many biological and technical surfaces significantly vary along different directions of a surface. This anisotropic frictional behavior may be induced by the crystal structure of a material, occurs on the surface of biological, composite or textile materials or may result from machining or finishing of a surface. If a body is sliding on a surface having anisotropic frictional properties, the magnitude of the friction force is dependent on the direction of sliding. In addition, it can be observed that without the presence of external forces, the sliding body is deflected. This phenomenon indicates that the friction force is not acting parallel to the sliding direction. Figure 1(a) shows an example of a sliding path of a polymer disc sliding on a horizontal steel plate, of which the surface has been ground in a fixed direction. For different initial sliding directions, the sliding disc is found to be deflected into the direction of the grooves caused by the grinding. Force laws describing anisotropic friction can be expressed using concepts of convex analysis. The constitutive behavior of stick and slip is thereby taken into account by formulating normal cone inclusion force laws [1, 2]. The shape of the friction force reservoir and the relationship between the sliding direction and the direction of the friction force is usually based on assumptions. In order to find accurate anisotropic friction force laws, the frictional behavior has to be examined experimentally. In this work, we define a force law which enables the description of a large class of anisotropic dry friction models and present experimental results of anisotropic friction measurements. In addition, the dissipativity and stability properties of the force law are examined. It is found, that the force law under certain conditions may lead to a type of frictional instability that until now has been ignored by the research community but is capable of causing anisotropic friction induced vibrations.

Anisotropic friction force laws

For an accurate description of the set-valued behavior of stick and slip, concepts of convex analysis can be used. We make use of the normal cone $\mathcal{N}_\mathcal{C}$ to a closed convex set $\mathcal{C}$ defined by $\mathcal{N}_\mathcal{C}(\boldsymbol{x}) = \{\boldsymbol{y} \mid \boldsymbol{y}^\mathrm{T}(\boldsymbol{x}^* - \boldsymbol{x}) \leq 0, \boldsymbol{x} \in \mathcal{C}, \forall \boldsymbol{x}^* \in \mathcal{C}\}$ [3]. The classical spatial Coulomb friction force law can be written as the normal cone inclusion

$$\boldsymbol{\gamma}_T \in \mathcal{N}_\mathcal{C}(-\boldsymbol{\lambda}_T), \tag{1}$$

where $\boldsymbol{\gamma}_T$ is the relative sliding velocity and $\boldsymbol{\lambda}_T$ is the friction force. In the isotropic case, the force reservoir $\mathcal{C}$ is a disc. This set-valued force law accounts for stiction, since the normal cone to a convex set is zero for any argument inside the set. The force law can be extended to anisotropic friction by using a force reservoir of elliptical or rectangular shape (see Fig. 1(b)) and assuming the principle of maximal dissipation to hold. But since the normal cone inclusion is only defined for convex sets $\mathcal{C}$, non-convex sets are not allowed. In [4] frictional anisotropy is modeled by uniformly distributed wedge-shaped asperities, where the faces of the asperities have isotropic friction properties. This model motivates the study of non-convex friction force reservoirs. For non-convex force reservoirs, the sliding direction can no longer be defined by normality to the force reservoir. Instead, a convex set $\mathcal{D}$ is introduced which specifies the sliding direction by normality.

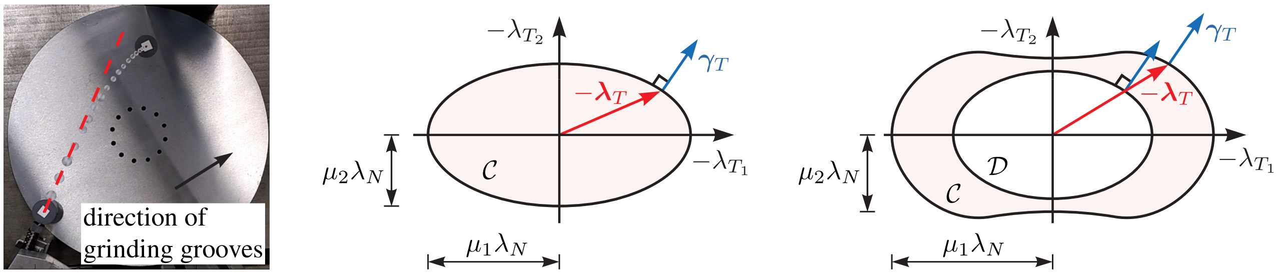

(a) (b) (c)

Figure 1: (a) Sliding path of a polymer disc on surface ground steel. (b) Graphical representation of the standard anisotropic friction force law and (c) the extended anisotropic friction force law.

A graphical representation of the force law is given in Fig. 1(c). Here, a generic non-convex force reservoir $\mathcal{C}$ and an elliptical set $\mathcal{D}$ are depicted. The symmetries with respect to the axes indicate an orthotropic force law. The friction coefficients along the semi-axes are μ_1 and μ_2, the normal force is called λ_N. The described force law can be expressed by a normal cone inclusion on the convex set $\mathcal{D}$ as

$$\boldsymbol{\gamma}_T \in \mathcal{N}_{\mathcal{D}}(-\alpha \boldsymbol{\lambda}_T). \tag{2}$$

The scaling parameter α is introduced to scale the friction force to the boundary of $\mathcal{D}$ during slip. This formulation allows for non-convex sets $\mathcal{C}$, as long as they are star-shaped with respect to the origin, and convex sets $\mathcal{D}$. Star-shaped sets fulfill the condition

$$\text{if} \quad \boldsymbol{x} \in \mathcal{C} \quad \text{then} \quad b\boldsymbol{x} \in \mathcal{C} \quad \forall b \in [0,1]\,. \tag{3}$$

The sets $\mathcal{C}$ and $\mathcal{D}$ can be described as the level sets of nonnegative, lower semicontinuous and positively homogeneous gauge functions $k_{\mathcal{C}}$ and $k_{\mathcal{D}}$ defined by $k_{\mathcal{C}}(\boldsymbol{x}) = \inf\{q > 0 \,|\, \boldsymbol{x} \in q\mathcal{C}\}$. The force reservoir is then given by $\mathcal{C} = \{-\boldsymbol{\lambda}_T \mid k_{\mathcal{C}}(-\boldsymbol{\lambda}_T) \leq 1\}$, i. e., the unit level set of the gauge function. Using the gauge functions, the scaling parameter α is specified by

$$\alpha = \frac{1}{k_{\mathcal{D}}(-\boldsymbol{\lambda}_T) - k_{\mathcal{C}}(-\boldsymbol{\lambda}_T) + 1} \tag{4}$$

such that

$$-\boldsymbol{\lambda}_T \in \operatorname{bdry} \mathcal{C} \quad \Rightarrow \quad -\alpha\boldsymbol{\lambda}_T \in \operatorname{bdry} \mathcal{D}. \tag{5}$$

In order to use a force law given as a normal cone inclusion for numerical simulations, the inclusion is rewritten as an implicit equation using a proximal point function. The contact problem is solved iteratively, where the parameter α is adapted in each iteration. For time integration, time-stepping methods can be used.

Dissipativity of friction force laws

The standard normal cone inclusion force law, with $\mathcal{C}$ being a closed conex set, can be rewritten using the subdifferential of the indicator function $\Psi_{\mathcal{C}}(-\boldsymbol{\lambda}_T)$ as $\boldsymbol{\gamma}_T \in \partial\Psi_{\mathcal{C}}(-\boldsymbol{\lambda}_T)$. The Fenchel equality [3] yields

$$-\boldsymbol{\lambda}_T^{\mathrm{T}}\boldsymbol{\gamma}_T = \Psi_{\mathcal{C}}(-\boldsymbol{\lambda}_T) + \Psi_{\mathcal{C}}^*(\boldsymbol{\gamma}_T). \tag{6}$$

The indicator function vanishes for all admissible friction forces. Therefore, only the support function $\Psi_{\mathcal{C}}^*(\boldsymbol{\gamma}_T)$ remains on the right hand side of Eq. (6). Since $\mathbf{0} \in \mathcal{C}$ it follows for the support function $\Psi_{\mathcal{C}}^*(\boldsymbol{\gamma}_T) \geq 0$ for all relative sliding velocities. The dissipation rate for the normal cone inclusion force law defined as $D = -\boldsymbol{\lambda}_T^{\mathrm{T}}\boldsymbol{\gamma}_T$ is thus positive.

The case of the extended normal cone inclusion force law Eq. (2) can be treated in an analogous fashion after analyzing the range of the scaling parameter α. For the gauge functions $k_{\mathcal{C}}$ and $k_{\mathcal{D}}$ the two conditions

$$-\boldsymbol{\lambda}_T \in \mathcal{C} \Rightarrow k_{\mathcal{C}}(-\boldsymbol{\lambda}_T) \leq 1, \tag{7}$$

$$k_{\mathcal{D}}(-\boldsymbol{\lambda}_T) \geq 0 \tag{8}$$

hold. During numerical simulations the case $-\boldsymbol{\lambda}_T \notin \mathcal{C}$ might occur. Without loss of generality of the force law we scale the set $\mathcal{D}$ such that $\mathcal{D} \subseteq \mathcal{C}$. It follows that $k_{\mathcal{D}}(-\boldsymbol{\lambda}_T) \geq k_{\mathcal{C}}(-\boldsymbol{\lambda}_T)$ which, using Eq. (4) leads to

$$0 < \alpha \leq 1. \tag{9}$$

Rewriting the normal cone inclusion Eq. (2) with the subdifferential of the indicator function and again using the Fenchel equality results in

$$\boldsymbol{\gamma}_T \in \partial\Psi_{\mathcal{D}}(-\alpha\boldsymbol{\lambda}_T) \;\Leftrightarrow\; -\alpha\boldsymbol{\lambda}_T \in \partial\Psi_{\mathcal{D}}^*(\boldsymbol{\gamma}_T) \;\Leftrightarrow\; -\alpha\boldsymbol{\lambda}_T^{\mathrm{T}}\boldsymbol{\gamma}_T = \underbrace{\Psi_{\mathcal{D}}(-\alpha\boldsymbol{\lambda}_T)}_{=0} + \Psi_{\mathcal{D}}^*(\boldsymbol{\gamma}_T). \tag{10}$$

As before, since the set $\mathcal{D}$ contains the zero element, it holds for the support function that $\Psi_{\mathcal{D}}^*(\boldsymbol{\gamma}_T) \geq 0$. Therefore, the dissipation rate for the extended friction force law is given by

$$D = -\boldsymbol{\lambda}_T^{\mathrm{T}}\boldsymbol{\gamma}_T = \frac{1}{\alpha}\Psi_{\mathcal{D}}^*(\boldsymbol{\gamma}_T) \geq 0. \tag{11}$$

The non-negative dissipation rate confirms that the presented friction force law is dissipative which is a necessary condition for a physically meaningful friction force law. Note that the dissipativity of the standard normal cone inclusion force law also directly follows from the maximal monotonicity of the force law. In the case of the extended force law, however, for $\mathcal{C} \neq c\mathcal{D}\ \forall c$, two pairs of $\boldsymbol{\lambda}_T$ and $\boldsymbol{\gamma}_T$ can be chosen such that

$$(-\boldsymbol{\lambda}_{T_{\mathrm{I}}} - (-\boldsymbol{\lambda}_{T_{\mathrm{II}}}))^{\mathrm{T}}(\boldsymbol{\gamma}_{T_{\mathrm{I}}} - \boldsymbol{\gamma}_{T_{\mathrm{II}}}) < 0. \tag{12}$$

Thus, the monotonicity and the stronger maximal monotonicity condition is not fulfilled for the extended friction law. Note that the extended friction law reduces to the standard friction law if $\mathcal{C} = c\mathcal{D}$ for some c.

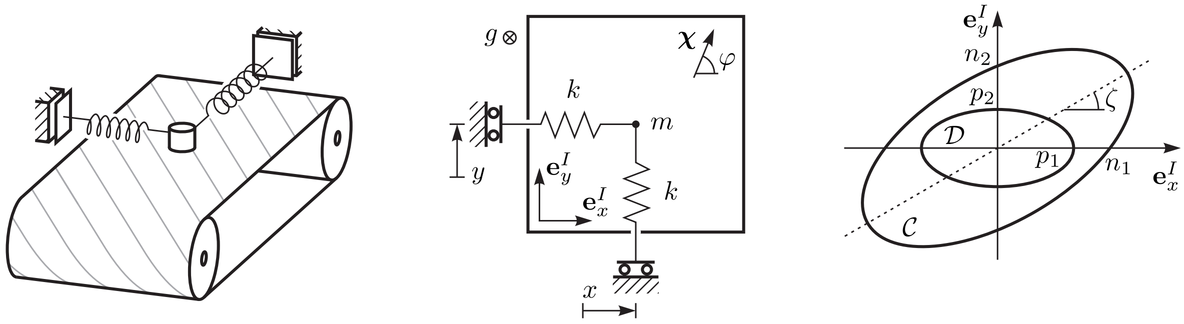

(a) (b) (c)

Figure 2: (a) Mass on belt with anisotropic friction properties. (b) Two degree of freedom model of the mass on belt. (c) Ellipsoidal sets defining the force law.

Anisotropic friction induced instability

Friction induced vibrations occur in many technical applications and are extensively studied in the literature. Many effects such as a dependency of the friction force on the magnitude of the sliding velocity or on the normal force in the contact point are identified to have an influence on the stability properties of dynamical systems with friction. In this work, we investigate the effects of anisotropic friction force laws on the stability of a sliding motion. The two degree of freedom system shown in Fig. 2(a) consists of a mass constrained by two linear springs, sliding on a horizontal belt having anisotropic friction properties. Figure 2(b) shows the top view of the model. The sliding body is modeled as a point mass on a surface moving constantly with velocity $\boldsymbol{\chi}$. The generalized coordinates are x and y along the axes $\mathbf{e}_x^I$ and $\mathbf{e}_y^I$. The equation of motion is given as

$$\boldsymbol{M}\ddot{\boldsymbol{q}} + \boldsymbol{K}\boldsymbol{q} = \boldsymbol{W}\boldsymbol{\lambda}_T, \tag{13}$$

where the generalized coordinates $\boldsymbol{q}$ and the diagonal mass matrix $\boldsymbol{M}$ and stiffness matrix $\boldsymbol{K}$ are

$$\boldsymbol{q} = \begin{pmatrix} x \\ y \end{pmatrix}, \quad \boldsymbol{M} = \begin{pmatrix} m & 0 \\ 0 & m \end{pmatrix}, \quad \boldsymbol{K} = \begin{pmatrix} k & 0 \\ 0 & k \end{pmatrix}. \tag{14}$$

The relative sliding velocity $\boldsymbol{\gamma}_T$ is given by the motion of the mass and the motion of the belt as $\boldsymbol{\gamma}_T = \boldsymbol{W}^{\mathrm{T}}\dot{\boldsymbol{q}} - \boldsymbol{\chi}$. The matrix of the generalized force direction $\boldsymbol{W}$ defined by $\boldsymbol{W} = (\partial\boldsymbol{\gamma}_T/\partial\dot{\boldsymbol{q}})^{\mathrm{T}}$ in this case is simply the identity matrix. For $\dot{\boldsymbol{q}} = \ddot{\boldsymbol{q}} = \boldsymbol{0}$ an equilibrium $\boldsymbol{q}^*$ is found. Since the belt is moving continuously ($\boldsymbol{\chi} \neq \boldsymbol{0}$) and with that the sliding velocity $\boldsymbol{\gamma}_T$ is nonzero, stick does not occur at the equilibrium. In the following, the stability of the equilibrium is analyzed for different force laws.

First, the standard normal cone inclusion force law $\boldsymbol{\gamma}_T \in \mathcal{N}_{\mathcal{C}}(-\boldsymbol{\lambda}_T)$ is considered. As mentioned above, the force law is maximal monotone, meaning that for all pairs $(\boldsymbol{\gamma}_T, \boldsymbol{\lambda}_T)$ and $(\boldsymbol{\gamma}_T^*, \boldsymbol{\lambda}_T^*)$ the condition

$$(\boldsymbol{\gamma}_T^* - \boldsymbol{\gamma}_T)^{\mathrm{T}} (-\boldsymbol{\lambda}_T^* - (-\boldsymbol{\lambda}_T)) \geq 0 \tag{15}$$

holds. We choose two solutions of Eq. (13) $\boldsymbol{q}_{\mathrm{I}}(t)$ and $\boldsymbol{q}_{\mathrm{II}}(t)$. The stability of the equilibrium can be determined by analyzing the distance between the two solutions. Introducing the incremental Lyapunov candidate function gives

$$V = \frac{1}{2}(\dot{\boldsymbol{q}}_{\mathrm{I}} - \dot{\boldsymbol{q}}_{\mathrm{II}})^{\mathrm{T}} \boldsymbol{M} (\dot{\boldsymbol{q}}_{\mathrm{I}} - \dot{\boldsymbol{q}}_{\mathrm{II}}) + \frac{1}{2}(\boldsymbol{q}_{\mathrm{I}} - \boldsymbol{q}_{\mathrm{II}})^{\mathrm{T}} \boldsymbol{K} (\boldsymbol{q}_{\mathrm{I}} - \boldsymbol{q}_{\mathrm{II}}). \tag{16}$$

Since $\boldsymbol{M}$ and $\boldsymbol{K}$ are positive definit, the Lyapunov candidate function V is PDF. Taking the time derivative and substituting Eq. (13) leads to

$$\begin{aligned} \dot{V} &= (\dot{\boldsymbol{q}}_{\mathrm{I}} - \dot{\boldsymbol{q}}_{\mathrm{II}})^{\mathrm{T}} \big(\boldsymbol{M}(\ddot{\boldsymbol{q}}_{\mathrm{I}} - \ddot{\boldsymbol{q}}_{\mathrm{II}}) + \boldsymbol{K}(\boldsymbol{q}_{\mathrm{I}} - \boldsymbol{q}_{\mathrm{II}})\big) \\ &= (\dot{\boldsymbol{q}}_{\mathrm{I}} - \dot{\boldsymbol{q}}_{\mathrm{II}})^{\mathrm{T}} (\boldsymbol{W}\boldsymbol{\lambda}_{T_{\mathrm{I}}} - \boldsymbol{W}\boldsymbol{\lambda}_{T_{\mathrm{II}}}) \\ &= \big(\boldsymbol{W}^{\mathrm{T}}(\dot{\boldsymbol{q}}_{\mathrm{I}} - \dot{\boldsymbol{q}}_{\mathrm{II}})\big)^{\mathrm{T}} (\boldsymbol{\lambda}_{T_{\mathrm{I}}} - \boldsymbol{\lambda}_{T_{\mathrm{II}}}) \\ &= (\boldsymbol{\gamma}_{T_{\mathrm{I}}} - \boldsymbol{\gamma}_{T_{\mathrm{II}}})^{\mathrm{T}} (\boldsymbol{\lambda}_{T_{\mathrm{I}}} - \boldsymbol{\lambda}_{T_{\mathrm{II}}}), \end{aligned} \tag{17}$$

where in the last step by subtracting the two solutions the velocity of the belt $\boldsymbol{\chi}$ cancels out. From the monotonicity condition of the force law Eq. (15) it follows that $\dot{V} \leq 0$. Therefore, V is a Lyapunov function which proves that the distance between two solutions is never increasing, i. e., the system is incrementally stable, implying that the equilibrium $\boldsymbol{q}^*$ is stable. Attractivity of the equilibrium is not shown and depends on additional damping in the system.

In the next step, instead of the standard normal cone inclusion force law, the extended force law Eq. (2) is applied. Since this force law is not maximal monotone the argumentation above is not valid. Instead, we study the particular case shown in Fig. 2(c). Here, the sets $\mathcal{C}$ and $\mathcal{D}$ are both ellipses with rotated semi-axes. The gauge functions of the sets are given by

$$k_{\mathcal{C}}(-\boldsymbol{\lambda}_T) = \sqrt{\left(\frac{\lambda_{T_1}}{n_1}\right)^2 + \left(\frac{\lambda_{T_2}}{n_2}\right)^2 + \nu\lambda_{T_1}\lambda_{T_2}}, \quad k_{\mathcal{D}}(-\boldsymbol{\lambda}_T) = \sqrt{\left(\frac{\lambda_{T_1}}{p_1}\right)^2 + \left(\frac{\lambda_{T_2}}{p_2}\right)^2}. \tag{18}$$

The force reservoir is an ellipse if the condition

$$\nu^2 < \frac{4}{n_1^2 n_2^2} \tag{19}$$

holds. The support function of the ellipsoidal set $\mathcal{D}$ is $\varPsi^*_{\mathcal{D}}(\boldsymbol{\gamma}_T) = \sqrt{(p_1 \gamma_{T_1})^2 + (p_1 \gamma_{T_1})^2}$. As before, an equilibrium can only occur during sliding. Therefore, for a smooth set $\mathcal{D}$ the friction force can be obtained from Eq. (10) as

$$-\boldsymbol{\lambda}_T = \frac{1}{\alpha} \left(\frac{\partial \varPsi^*_{\mathcal{D}}(\boldsymbol{\gamma}_T)}{\partial \boldsymbol{\gamma}_T} \right)^{\mathrm{T}}, \tag{20}$$

where the set-valued subdifferential is replaced by the gradient. During sliding the friction force is at the boundary of the force reservoir $\mathcal{C}$ and $k_{\mathcal{C}}(-\boldsymbol{\lambda}_T) = 1$. Evaluating the gauge function with Eq. (20) and making use of the fact that the gauge function is positively homogeneous, the friction force during slip is found as a function of $\boldsymbol{\gamma}_T$

$$-\boldsymbol{\lambda}_T = \frac{1}{\beta(\boldsymbol{\gamma}_T)} \begin{pmatrix} p_1^2 \gamma_{T_1} \\ p_2^2 \gamma_{T_2} \end{pmatrix}, \tag{21}$$

with the scalar function

$$\beta(\boldsymbol{\gamma}_T) = \varPsi^*_{\mathcal{D}}(\boldsymbol{\gamma}_T) k_{\mathcal{C}} \left(\left(\frac{\partial \varPsi^*_{\mathcal{D}}(\boldsymbol{\gamma}_T)}{\partial \boldsymbol{\gamma}_T} \right)^{\mathrm{T}} \right) = \sqrt{\left(\frac{p_1^2}{n_1} \gamma_{T_1} \right)^2 + \left(\frac{p_2^2}{n_2} \gamma_{T_2} \right)^2 + \nu \left(p_1^2 p_2^2 \gamma_{T_1} \gamma_{T_2} \right)}. \tag{22}$$

The equilibrium of the system is found at $\boldsymbol{q}^* = \boldsymbol{K}^{-1} \boldsymbol{W} \boldsymbol{\lambda}_T$. We study the stability of the equilibrium by an eigenvalue analysis of the linearized system

$$\boldsymbol{M} \ddot{\boldsymbol{q}} + \boldsymbol{B} \dot{\boldsymbol{q}} + \boldsymbol{K}(\boldsymbol{q} - \boldsymbol{q}^*) = \boldsymbol{0}. \tag{23}$$

The damping matrix $\boldsymbol{B}$ is thereby obtained by

$$\boldsymbol{B} = -\boldsymbol{W} \frac{\partial \boldsymbol{\lambda}_T}{\partial \boldsymbol{\gamma}_T} \boldsymbol{W}^{\mathrm{T}} = \frac{p_1^2 p_2^2}{\beta(\boldsymbol{\gamma}_T)^3} \begin{pmatrix} \frac{p_2^2}{n_2^2} \gamma_{T_2}^2 + \frac{1}{2} \nu p_1^2 \gamma_{T_1} \gamma_{T_2} & -\frac{p_2^2}{n_2^2} \gamma_{T_1} \gamma_{T_2} - \frac{1}{2} \nu p_1^2 \gamma_{T_1}^2 \\ -\frac{p_1^2}{n_1^2} \gamma_{T_1} \gamma_{T_2} - \frac{1}{2} \nu p_2^2 \gamma_{T_2}^2 & \frac{p_1^2}{n_2^2} \gamma_{T_1}^2 + \frac{1}{2} \nu p_2^2 \gamma_{T_1} \gamma_{T_2} \end{pmatrix} \tag{24}$$

at $\dot{\boldsymbol{q}} = 0$ with $\boldsymbol{W}$ being the identity matrix. The damping matrix is singular, $\det(\boldsymbol{B}) = 0$ and in general nonsymmetric. The eigenvector of the zero eigenvalue ϵ_1 is collinear to the sliding direction. The second eigenvalue ϵ_2 is determined by the trace of $\boldsymbol{B}$,

$$\epsilon_2 = \frac{p_1^2 p_2^2}{\beta(\boldsymbol{\gamma}_T)} \left(\frac{p_1^2}{n_1^2} \gamma_{T_1}^2 + \frac{p_2^2}{n_2^2} \gamma_{T_2}^2 + \frac{1}{2} \nu \left(p_1^2 + p_2^2 \right) \gamma_{T_1} \gamma_{T_2} \right). \tag{25}$$

The corresponding eigenvector is tangent to the boundary of the force reservoir $\mathcal{C}$ at $-\boldsymbol{\lambda}_T$. The sign of the eigenvalue ϵ_2 determines whether the damping matrix is positive or negative semidefinit. For a positive semidefinit damping matrix the energy in the system can be used as Lyapunov function to show the stability of the equilibrium $\boldsymbol{q}^*$ of the linear system Eq. (23). For a negative eigenvalue ϵ_2 the damping matrix $\boldsymbol{B}$ becomes negative semidefinit. The eigenvalue can become negative if

$$\nu^2 > \frac{16 p_1^2 p_2^2}{(p_1^2 + p_2^2)^2 (n_1^2 n_2^2)}. \tag{26}$$

For ν fulfilling conditions Eq. (19) and Eq. (26), sliding directions $\boldsymbol{\gamma}_T$ exist such that eigenvalue ϵ_2 is negative. The system can be rewritten in first order form with the system matrix

$$\boldsymbol{A} = \begin{pmatrix} \boldsymbol{0} & \mathbf{I} \\ -\boldsymbol{M}^{-1} \boldsymbol{K} & -\boldsymbol{M}^{-1} \boldsymbol{B} \end{pmatrix}. \tag{27}$$

Choosing the simple case of $\boldsymbol{M}$ and $\boldsymbol{K}$ being identity matrices, it can be shown that a negative eigenvalue of $\boldsymbol{B}$ leads to an eigenvalue with positive real part of the system matrix $\boldsymbol{A}$ which proves instability of the equilibrium.

As an example we consider the mass on belt system with the force law with two elliptical sets both having the semi-axes ratio $3/1$ where the semi-axes of the force reservoir are rotated by the angle ζ. From condition Eq. (26) it follows that instability can occur for $17.1° < \zeta < 72.9°$. If the rotation angle is set to $\zeta = 30°$, then the range of the directions of motion of the belt for which the eigenvalue ϵ_2 becomes negative and the equilibrium becomes unstable lies between $44.1° < \varphi < 75.9°$. The angle φ determines the moving direction of the belt as shown in Fig. 2(b). A graphical representation of the force law is given in Fig. 3(a). The critical sliding directions for which instability occurs are those where the vector of the sliding direction points into the set $\mathcal{C}$. At the values of φ given above, the sliding velocity is tangent to the force reservoir. Figure 3(b) shows the bifurcation diagram of the magnitude of the equilibrium position as a function of the direction of the belt movement. The solid line marks the stable solutions. For angles in the critical interval, the equilibrium is unstable and the mass on the belt starts to vibrate if a small perturbation is applied. After some time the solution approaches a stable limit cycle. An example for a limit cycle for $\varphi = 50°$ is given in Fig. 3(c). It is calculated using Moreau's timestepping scheme [5]. The belt velocity is chosen low. Therefore, the mass sticks to the belt during each cycle which results in the straight line in the limit cycle. For higher belt velocities limit cycles without stiction are observed.

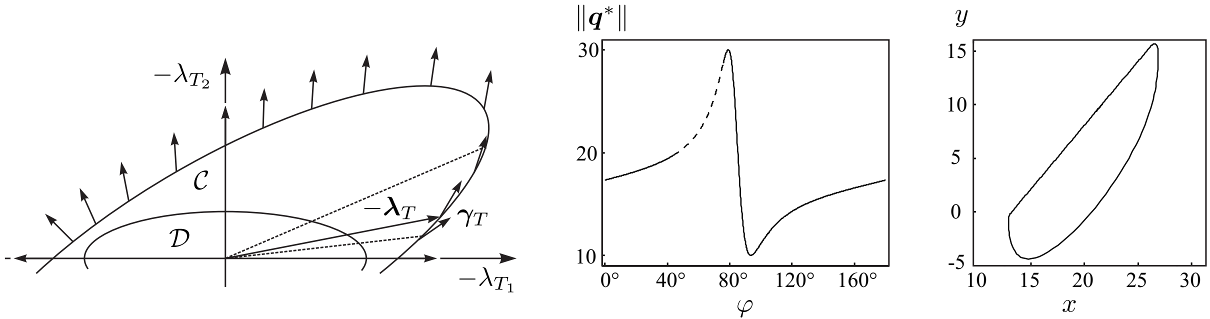

(a) (b) (c)

Figure 3: (a) Graphical representation of force law with rotated sets. (b) Bifurcation diagram of the equilibrium. (c) Limit cycle of the mass on the belt for $\varphi = 50°$.

Experimental work

In the literature various experimental studies of anisotropic friction can be found. However, the friction force is often only measured in the direction of sliding. Movement in the direction orthogonal to the sliding direction is often constraint without measurement of the force. Since the friction force in the case of anisotropic surfaces is not necessarily collinear to the sliding direction, the frictional behavior can only be analyzed accurately by measuring the friction forces in two directions. To describe spatial anisotropic friction, the relationship between the sliding direction and the friction force has to be determined experimentally for all possible sliding directions.

Experimental setup and data analysis

The experimental setup shown in Fig. 4(a) makes use of a spinning anisotropic surface and a stationary pin (pin-on-disc). Unlike in many pin-on-disc-tribometers, the friction force is measured in two orthogonal directions and the rotation angle of the disc is recorded. This setup allows to observe the friction forces for all possible sliding directions during one full rotation of the disc. The steel disc (diameter $30\,\mathrm{cm}$) is driven with a synchronous servomotor with a harmonic drive gear unit. The output of the motor is $690\,\mathrm{W}$ and the disc can be driven in both directions with a maximum speed of $200\,\mathrm{rpm}$. The normal force is applied using weights that are placed on a linear ball spline shaft. The friction forces in tangential and radial direction of the disc, as well as the normal force are measured using a 3D force sensor. Various contact partners can be tested. The pins mounted on the force sensor are made of different materials and have cylindrical or hemispherical shapes. The contact area between the rotating disc and the pins is small. Thus, the influence of varying sliding velocities along the radius of the disc which leads to combined sliding and drilling friction is minimized. For each measurement, the contact partners, normal force and sliding velocity have to be defined. During a measurement, the time signals of the friction forces in radial and tangential direction, the normal force and the rotation angle of the disc are recorded.

The goal of the measurement is to determine the shapes of the sets $\mathcal{C}$ and $\mathcal{D}$. The friction forces λ_r and λ_t are measured in the I-frame of the sensor in radial and tangential direction of the disc. The forces are transformed into the co-rotating frame K of the disc with the known current rotation angle φ of the disc (see Fig. 4(b)). Plotting the transformed forces in a diagram gives discrete points on the boundary of the force reservoir $\mathcal{C}$. The extended normal cone inclusion force law Eq. (2) makes use of the force reservoir $\mathcal{C}$ and a second set $\mathcal{D}$. The sliding direction is defined by normality to the set $\mathcal{D}$. In the described experimental setup the relative sliding velocity is known to point in tangential direction of the rotating disc. Points on the boundary of $\mathcal{D}$ are addressed with the vector $\boldsymbol{r}_{\mathcal{D}}$ as shown in Fig. 4(c). Since $\boldsymbol{\gamma}_T$ is normal to $\mathcal{D}$, the condition

$$\boldsymbol{r}'_{\mathcal{D}}(\theta) \perp \boldsymbol{\gamma}_T \quad \Leftrightarrow \quad \boldsymbol{r}'_{\mathcal{D}}(\theta) \cdot \boldsymbol{\gamma}_T = 0 \tag{28}$$

has to be met, where the prime indicates differentiation with respect to θ. After some manipulation the first order homogeneous differential equation

$$r'_{\mathcal{D}}(\theta) - \tan(\theta - \varphi) r_{\mathcal{D}}(\theta) = 0. \tag{29}$$

for the magnitude of $\boldsymbol{r}_{\mathcal{D}}$ is obtained. A solution is found by separation of variables and integration giving

$$r_{\mathcal{D}}(\theta) = r_{\mathcal{D}}(0) \mathrm{e}^{\int_0^\theta \frac{\lambda_r}{\lambda_t} \mathrm{d}\tilde{\theta}}. \tag{30}$$

Using (30), points on the boundary of the set $\mathcal{D}$ can be calculated. To be able to formulate the force law according to Eq. (2) the sets have to fulfill certain conditions. The normal cone is only defined to convex sets, therefore the set $\mathcal{D}$ must be convex. The scaling of the set, given by $r_{\mathcal{D}}(0)$, is arbitrary. For numerical treatment, where the normal cone inclusion is rewritten as implicit proximal point function, it is advantageous to scale the set $\mathcal{D}$ such that it is in the interior of the force reservoir $\mathcal{C}$. The force reservoir $\mathcal{C}$ has to be star-shaped, so that uniqueness is guaranteed, but does not necessarily need to be convex.

Experimental results

The experiment is performed for different material combinations. First, an isotropic surface is tested. Isotropic frictional behavior can be achieved by sandblasting a steel surface, thereby creating randomly distributed microscopic asperities.

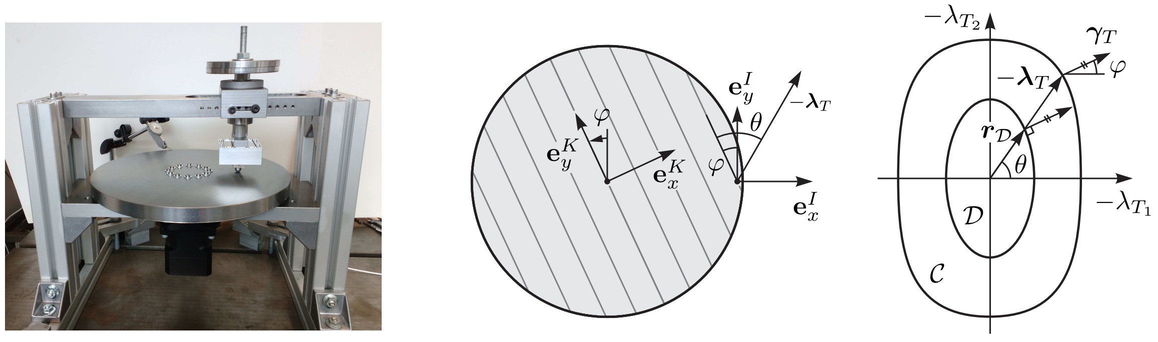

(a) (b) (c)

Figure 4: (a) Experimental setup for the measurement of the friction forces. (b) Top view of the rotating disc with coordinate frames. (c) Calculated sets $\mathcal{C}$ and $\mathcal{D}$.

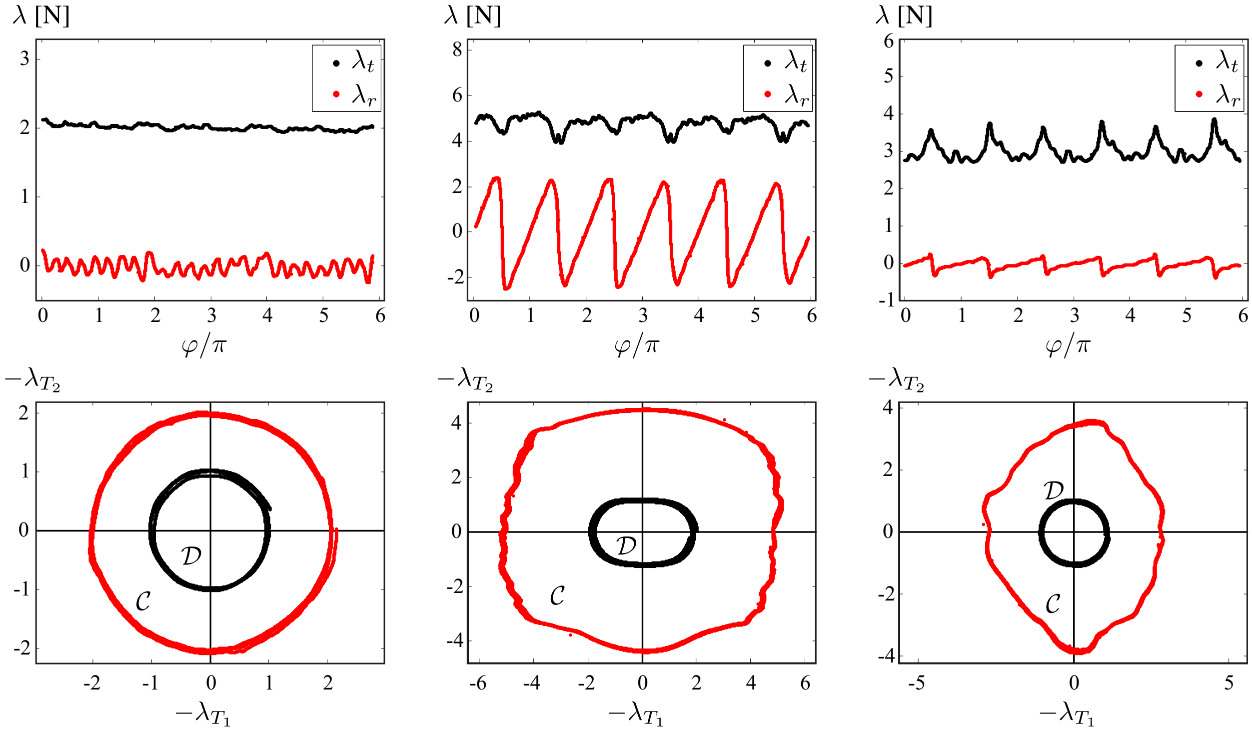

(a) (b) (c)

Figure 5: Top row: measured friction forces in tangential and radial direction, bottom row: calculated sets $\mathcal{C}$ and $\mathcal{D}$ for (a) steel pin on sandblasted steel disc, (b) rubber pin on surface ground disc, (c) steel pin on surface ground disc.

A hemispherical steel pin is pressed against the disc with a normal force of $\lambda_N = 14.0\,\mathrm{N}$. The relative sliding velocity determined by the rotation speed of the disc and the pin position is set to $\|\gamma_T\| = 50\,\frac{\mathrm{mm}}{\mathrm{s}}$. Figure 5(a) shows the measured friction forces in tangential and radial direction for three full rotations of the disc. The tangential force is constant, while the radial force is approximately zero. Small deviations are caused by irregularities of the surface. As expected for an isotropic material, the calculated force reservoir $\mathcal{C}$ and the set $\mathcal{D}$ are circles. Therefore, for isotropic frictional behavior the standard normal cone inclusion force law Eq. (1) with a circular force reservoir is sufficient. Since the magnitude of the friction force is independent of the sliding direction, a single value for the friction coefficient can be determined as $\mu \approx 0.14$.

Next, an example of an anisotropic surface is studied. A steel disc is surface ground such that all grinding grooves are parallel. Measurements with two different contact partners are performed. In Fig. 5(b) the results for a cylindrical rubber pin with a diameter of $7\,\mathrm{mm}$, a normal force of $\lambda_N = 9.3\,\mathrm{N}$ and a sliding velocity of $\|\gamma_T\| = 50\,\frac{\mathrm{mm}}{\mathrm{s}}$ are shown. The friction forces show a periodicity with two maximums per full rotation of the disc. This behavior is expected for an orthotropic surface due to symmetry. The tangential force component oscillates around a constant offset, while the radial force component shows a sawtooth oscillation around zero. A similar behavior is found in [6]. Maximum and minimum values of the tangential force occur at zero crossings of the radial force. For $\varphi = k\pi$ the pin is sliding orthogonal to the grinding grooves and the tangential force is maximal. When the pin is sliding along the grooves, the tangential force is minimal. The resulting sets significantly differ from the circular shape in the isotropic case. Both sets are rounded rectangles. A standard ellipse, as is often assumed for the force reservoir in the case of anisotropic friction in the literature,

does not accurately describe the experimentally determined sets. The friction coefficients for sliding directions orthogonal and parallel to the grinding grooves are $\mu_1 \approx 0.55$ and $\mu_1 \approx 0.48$, respectively.
In addition, the experimental results obtained using a hemispherical steel pin with a normal force of $\lambda_N = 18.5\,\mathrm{N}$ and a sliding velocity of $\|\gamma_T\| = 100\,\frac{\mathrm{mm}}{\mathrm{s}}$ are shown in Fig. 5(c). Again, the tangential component oscillates around a non-zero mean value, while the radial component shows a sawtooth behavior. However, the maximum values of the tangential force occur during sliding along the grinding grooves. This leads to the shown calculated sets. The shapes of $\mathcal{C}$ and $\mathcal{D}$ substantially differ from each other. This behavior can not be represented by the standard normal cone inclusion force law Eq. (1). The extended normal cone inclusion force law Eq. (2), where $\mathcal{C}$ and $\mathcal{D}$ are independent of one another, however, gives an accurate description of the frictional behavior.

Conclusions

The proposed extended normal cone inclusion force law for anisotropic friction allows for non-convex star-shaped force reservoirs. While force laws based on maximal dissipation do not lead to anisotropic friction induced vibration, the extended force law is capable of causing instabilities for certain parameters. The presented experimental setup can be used to analyze the magnitude and direction of the friction force for various contact partners. Using the measurement results different shapes of the force reservoirs are obtained. The described normal cone inclusion force law in combination with the experimentally measured sets enables the accurate representation of the complex behavior of anisotropic friction.

References

[1] Leine R.I., van de Wouw N. (2008) *Stability and Convergence of Mechanical Systems with Unilateral Constraints*, vol. 36 of *Lecture Notes in Applied and Computational Mechanics*. Springer, Berlin.

[2] Walker S.V., Leine R.I. (2016) Modeling and numerical simulation of anisotropic dry friction with non-convex friction force reservoir. in *Proc. IMSD*, Montréal.

[3] Rockafellar R.T., Wets R.J.-B. (1998) *Variational Analysis*. Springer, Berlin.

[4] Michalowski R., Mróz Z. (1978) Associated and non-associated sliding rules in contact friction problems. *Archiv. Mech.* **30**:259-276.

[5] Moreau J.J. (1988) *Unilateral contact and dry friction in finite freedom dynamics* In: *Nonsmooth Mechanics and Applications*. Springer, Wien.

[6] Tapia F., Le Tourneau D., Géminard J.-C. (2016) Anisotropic friction: assessment of force components and resulting trajectories. *EPJ Techniques and Instrumentation* **3**:1-10.